UNIVERSITÉ
LAVAL

Templated dewetting for self-assembled ultra-low-loss chalcogenide integrated photonics

Philippe Jean, Alexandre Douaud, Sophie LaRochelle, Younès Messaddeq, and Wei Shi

Templated dewetting for self-assembled ultra-low-loss chalcogenide integrated photonics

PHILIPPE JEAN,[1,2] [iD] ALEXANDRE DOUAUD,[1] [iD] SOPHIE LAROCHELLE,[1,2] YOUNÈS MESSADDEQ,[1,3] AND WEI SHI[1,2,*] [iD]

[1] *Centre d'Optique, Photonique et Laser (COPL), 2375 rue de la Terrasse, Université Laval, Québec, G1V 0A6, Canada*

[2] *Département de Génie Électrique et de Génie Informatique, Université Laval, 2325, rue de l'Université, Québec, G1V 0A6, Canada*

[3] *Département de Physique, de Génie Physique et d'Optique, Université Laval, 2325, rue de l'Université, Québec, G1V 0A6, Canada*

wei.shi@gel.ulaval.ca

Abstract: Integrated photonics is of growing interest but relies on complex fabrication methods that have yet to match optical losses of bulkier platforms like optical fibers or whispering gallery mode resonators. Spontaneous matter reorganization phenomenon (e.g. dewetting) in thin-films provides a way for self-assembled structures with atomic scale surface rugosity, potentially alleviating the problems of roughness scattering loss and fabrication complexity. In this article, we study solid-state dewetting in chalcogenide glass thin-films and demonstrate its applicability to the fabrication of high-quality integrated photonics components. Optimal dewetting parameters are derived from a comprehensive experimental study of thin-film properties under high temperature rapid annealing. Atomic scale surface roughness are obtained using dewetting, with RMS values as low as $R_q = 0.189$ nm. Several integrated photonics components are fabricated using the method and characterized. We show that the use of pre-patterned templates leads to organized, reproducible patterns with large-scale uniformity and demonstrate the record high quality-factor of 4.7×10^6 in compact ($R = 50 \, \mu$m) microdisks, corresponding to $0.08 \, \text{dB} \cdot \text{cm}^{-1}$ waveguide propagation loss. The integrated devices are directly fabricated on standard silicon-on-insulator dice using the micro-trench filling technique and coupled to silicon waveguides, making them readily deployable with existing silicon devices and systems.

1. Introduction

In recent years, the down-scaling of bulk optical components onto the chip scale has been a major part of photonics research. Integrated photonics now enables increased complexity in systems through the combination of hundres of ultra-small components on cm-scale dice [1] and is instrumental in the development of fundamentally important fields like telecommunications [2] and quantum computing [3]. Improvement in the fabrication methods of those micro- and nano-scale components is a major driving factor behind integrated photonics progress [4–6]. The current fabrication paradigm relies on a combination of lithography and material etching. This approach allows for large design freedom, nanometer-scale components and, given ample efforts and cost, ultra-low-loss waveguides [4,7]. Yet, direct etching of the waveguide material inevitably leaves ultra-small defects that cause Rayleigh scattering and important optical loss [8]. Getting rid of these defects requires modification of the surface morphology through heavy post-etch processing. This is often accomplished with intensive multi-days annealings steps at high temperatures($T > 1000 \,°$C) or chemical-mechanical polishing steps [6,9]. These additional steps not only increase the fabrication complexity and cost but often sacrifice compatibility with

the ubiquitous complementary metal-oxide-semiconductor (CMOS) fabrication process. There is then a need to devise innovative microfabrication techniques that can address those drawbacks while retaining the CMOS compatibility.

The phenomenon of spontaneous matter reorganization could lead to substantial improvement in surface morphology of integrated devices at little processing cost. Furthermore, this phenomenon enables the fabrication of self-assembled structures, thus reducing process complexity [10,11]. Spontaneous reorganization occurs when matter is reflowed by interfacial forces towards an equilibrium shape where energy is minimized [11]. Laser induced reflow of silicon dioxide microtoroids and microlenses is a prime example that led to substantial improvement and spurred the development of a high-impact research field on ultra-high-Q microresonators [12,13]. To translate these advantages to CMOS photonics, spontaneous matter reorganization must be applied at the wafer-scale to thin-films on silicon dioxide substrates at moderate temperatures ($T <$ 500 °C). Thermally induced dewetting, where a heated thin-film dewets from its substrate and agglomerates, can provide the required dynamics to leverage spontaneous matter reorganization in integrated optics. The potential of dewetting to generate large-scale, uniform, self-assembled structures has been outlined in work focused in microlenses arrays on planar substrates [10,14]

The main conditions for dewetting are a low viscosity and an adequate difference in surface tension between the thin-film and its substrate. Low viscosities can be easily obtained with sufficiently high temperatures, however, glassy materials must possess a large $\Delta T = T_x - T_g$ in order to remain amorphous during annealing. Among the materials suitable for dewetting at CMOS-compatible temperatures, chalcogenide glasses are particularly attractive because of their exceptional optical properties [15]. They also undergo solid-state dewetting [16,17], which mean that they remain in their solid phase throughout the process. Their high refractive index, large χ^3 nonlinearity, broad transparency window, phase-change properties, photo-induced effects have made chalcogenide glasses some of the most used and studied materials in integrated photonics [18–22]. Chalcogenides have moderate glass transition temperature (T_g) and sometimes high or nonexistent cristallization temperatures (T_x), making them resilient to the high-temperature rapid annealing required to induce dewetting. High-quality chalcogenide waveguides are notoriously difficult to achieve and could benefit from improved fabrication techniques [23].

In this work, we present a comprehensive study of the dewetting phenomenon in $As_{20}S_{80}$ thin-films and its application to hybrid chalcogenide-silicon integrated photonics. The effect of temperature and time on the thin-film properties are investigated to find an optimal window for the dewetting treatment. A short annealing (30 s) at CMOS-compatible temperatures between 220 °C and 240 °C is shown to provide the best results. These parameters result in an atomic-scale surface roughness of $R_q <$ 2 Å and an evolution of the thin-film properties towards those of the bulk state. The process is then applied to the fabrication of several integrated photonics components using the micro-trench filling technique for heterogeneous integration on the silicon-on-insulator (SOI) platform. This approach provides CMOS-compatible devices that can be seamlessly interfaced with existing silicon components and optical fibers. Low propagation loss of 0.38 dB·cm^{-1} are measured in high confinement waveguides. Quality factors up to 4.7×10^6 are reported in compact ($R \leq 50$ μm) microdisks — the largest reported quality factor in a sub-mm planar chalcogenide microresonator to-date. The results of this work propose a novel avenue towards leveraging spontaneous matter reorganization for integrated photonics. Also, this work represent a significant contribution to the understanding of the dewetting phenomenon and how it can be applied for practical and useful applications and indicates that dewetting is a suitable microfabrication technique that can improve existing methods and provide a path for novel process.

This article is organized as follow. In Section 3, the effect of high-temperature rapid annealing on thin-film properties are investigated. In Section 4, the technique of templated dewetting as applied for integrated photonics is described and supported by the experimental demonstration of several integrated components. Section 5 discusses the scope of this work within the existing

literature and the current limitations. Finally, a brief conclusion provides perspective on future applications and work.

2.　Methods

2.1.　Glass preparation

The $As_{20}S_{80}$ bulk glass was prepared by the melt-quenching technique, from intensely purified arsenic and sulfur, sealed in an evacuated silica tube. The resulting glasses were further purified by distillation with in-house recipes, in order to obtain highly purified optical materials.

2.2.　Thin-film deposition

$As_{20}S_{80}$ thin-films were deposited on fused silica slides (25 mm×25 mm) and silicon chips. A Nanochrome device (IntlVac), equipped with an electron beam source was used to evaporate the As–S glasses. For the deposition, the chamber was evacuated down to approximately 1×10^{-6} Torr, and a rotation of 80 rpm was used for the substrates holder to ensure homogeneous films. An evaporation rate of $10\,\text{Å·s}^{-1}$ was chosen for its ideal results and the thickness of the thin-films range from 1.00 µm to 1.15 µm. All the devices in this work were cladded with a 50 nm silicon dioxide passivation film to prevent surface oxidation. The passivation film was deposited using the same Nanochrome evaporator, with a deposition rate of $5\,\text{Å·s}^{-1}$.

2.3.　Thermal treatments

In order to induce thermal dewetting of the thin-films, a Rapid Thermal Annealing (RTA) oven was used to heat the samples from room temperature up to 340 °C at a heating rate of $100\,°\text{C·min}^{-1}$. The RTA oven uses an inert atmosphere composed of a mixture of argon and nitrogen (Ar/N_2, 10 sccm each) to avoid any detrimental surface crystallization due to oxygen (formation of As_2O_3 crystals). A list of all thermal treatments is presented in Table 1.

Table 1. Summary of thermal treatments done to thin-films deposited on silica substrates. All of them were performed under inert atmosphere (Ar/N_2), using a heating rate of 100 °C·min^{-1}.

Duration: 30 s						
100 °C	120 °C	140 °C	160 °C	180 °C	200 °C	220 °C
240 °C	260 °C	280 °C	300 °C	320 °C	340 °C	
Duration: 120 s						
100 °C	120 °C	140 °C	160 °C	180 °C	200 °C	220 °C
240 °C	260 °C	280 °C	300 °C	320 °C	340 °C	

2.4.　Composition analysis

A Scanning Electron Microscope (SEM) (FEI, model Quanta 3D FEG) coupled to Energy Dispersive X-ray spectroscopy (EDX) was used to analyse the surface morphology and to provide quantitative compositional information of thin-films deposited on silica substrates (without a SiO_2 passivation layer on top of the thin-film), respectively. Both SEM images and EDX measurements were performed under low vacuum (with H_2O vapour). EDX scans were executed with an acceleration voltage of 20 kV, and analysis lines of K_α and L_α for As, and K_α for S. A correcting factor, extracted from an $As_{20}S_{80}$ bulk reference, was applied to the raw data to compensate for the variation in sulfur caused by the depth of analysis.

2.5.　Surface morphology

The roughnesses of the thin-films deposited on silica substrates (without a SiO_2 passivation layer on top of the thin-film) were measured with the help of Atomic Force Microscopy (AFM,

diDimension V SPM model from Veeco) in tapping mode. To calculate the root mean squared roughness (R_q) as well as the arithmetic average roughness (R_a), an area of $1\,\mu m^2$ was measured for each sample, with a scanning speed of $1.67\,\mu m \cdot s^{-1}$ (0.6 Hz).

2.6. Structural study

We performed structural analysis of the thin-films deposited on silica substrates (without a SiO_2 passivation layer on top of the thin-film) using micro Raman spectroscopy (Renishaw inVia model) coupled with a Leica DM2700 microscope. A backscattering geometry was used in the frequency range of $100–600\,cm^{-1}$, with a $1200\,line \cdot mm^{-1}$ grating. The excitation light source was a 785 nm laser, operating at approximately 76 mW. Each spectrum is the sum of 3 acquisition of 5 s done in dynamic mode, *i.e.*, the surface was scanned during measurement instead of doing a static acquisition of the same point ; this method allows the use of more power to get a better signal to noise ratio, without modifying or damaging the surface. In addition, very low power scans were also performed to ensure the validity of this method, as chalcogenide glasses are quite sensitive to photo-induced surface modifications. The wave number uncertainty was estimated to be $\pm 2\,cm^{-1}$.

2.7. Refractive index characterization

Both refractive indices and thicknesses of the thin-films deposited on silica substrates (without a SiO_2 passivation layer on top of the thin-film) were measured via the prism-coupling technique using a Metricon 2010/M Prism Coupler linked to five lasers operating at 532, 633, 972, 1308 and 1538 nm. For this study, however, only laser sources of 633, 972, 1308 and 1538 nm were used for $As_{20}S_{80}$, as light sources with lower wavelengths (close to the bandgap) tend to induce a photo-darkening effect (among others), rendering results untrustworthy. The refractive index uncertainty is estimated to be $\pm 5 \times 10^{-4}$.

2.8. Optical measurements

The optical transmissions of the fabricated devices were measured using an Agilent mainframe (8164A) with a photodetector (81635A) and a tunable laser (81640B). Light was coupled to and from the silicon waveguides using inverse tapers (180 nm wide, $100\,\mu m$ long) and tapered single-mode fibers ($2.5\,\mu m$ mode field diameter) from OZOptics. A polarization controller paddle was used to control the polarization state at the input of the chip. All measurements were done with the input light aligned on the quasi-TE axis of the silicon waveguide. The data obtained from the optical measurements was analyzed using Python scripts developed by the authors.

2.9. SOI chips fabrication

The chips were processed by Advanced MicroFoundry (AMF, Singapore) using 193 nm photolithography on 200 mm SOI wafers. The buried oxide layer (BOx) thickness was $3\,\mu m$. The micro-trenches were defined in-foundry as part of the AMF process. The remainder of the fabrication process details are proprietary to AMF. The die-level micrographs of the chips were taken using an optical microscope. The cross-section images were taken using an SEM and by manually cleaving the chips. The typical silicon waveguide loss according to the manufacturer is $1.5\,dB \cdot cm^{-1}$. Before thin-film deposition, the chips were treated to a 10 s buffered oxide etchant (BOE) dip to reduce silica rugosity.

2.10. Quality factor

The quality factors of the resonators were extracted directly from the transmittance spectrum using curve fitting with a Lorentzian function for the single peaked resonance and a double

Lorentzian function for the dual peaked resonance. For the splitted resonances, if we assume symmetric resonance, the fitting function is expressed as:

$$T(\omega) = A_0 - \frac{T_0(\delta\omega/2)^2}{(\omega - \omega_{r1})^2 + (\delta\omega/1)^2} - \frac{T_0(\delta\omega/2)^2}{(\omega - \omega_{r2})^2 + (\delta\omega/2)^2} \tag{1}$$

where A_0 is a normalization factor that accounts for the insertion loss, $\delta\omega$ is the resonance FWHM linewidth and $\omega_{r1,r2}$ are the resonance angular frequencies. In the case of a single peak, the fitting function reduces to:

$$T(\omega) = A_0 - \frac{T_0(\delta\omega/2)^2}{(\omega - \omega_r)^2 + (\delta\omega/2)^2} \tag{2}$$

The linewidth and the resonant angular frequency of the resonance are then used to calculate the loaded quality factor $Q_l = \omega_r/\delta\omega$. The intrinsic quality factors are obtained by assuming undercoupling [24,25]:

$$Q_i = \frac{2Q_l}{1 + \sqrt{T_0}} \tag{3}$$

where T_0 is the relative transmittance at resonance. From the intrinsic quality factor, we can approximate the waveguide propagation loss as [26]:

$$\alpha = \frac{\omega_r}{v_g Q_i} \tag{4}$$

where $v_g = c/n_g$ is the group velocity.

Those high-Q resonances exhibit strong frequency splitting. This effect appears when the clockwise (CW) and counterclockwise (CCW) waves couples through scattering from the sidewalls and the coupler [27]. The frequency splitting strength depends on many factors and is partly stochastic, which explains the different splitting observed between devices and at different wavelengths.

3. Thin-films characterization

This section study the effects of thermal treatment on different properties of $As_{20}S_{80}$ thin-films. Thermally induced dewetting requires a fine balance between a high enough temperature to induce film breakup while preventing undesirable material evaporation. The goal of this section is to identify the optimal parameters range for dewetting. To do so, we prepared 27 thin-film samples directly on silica substrates (glass slides). We used one sample for as-deposited characterizations while the other 26 were dedicated to annealings with 13 temperatures and 2 annealing times. The annealings durations are 30 s and 120 s, and the temperatures range from 100 °C to 340 °C with steps of 20 °C. Different heating rates ranging from 10 °C·min^{-1} to 100 °C·min^{-1} were tested: using low heating rates caused the dewetting to be inhomogeneous and lead to the evaporation of matter at high temperatures, whereas using a high heating rate caused the thin-film to dewet homogeneously with a uniform matter reflow across the whole waveguide, and allowed the use of higher temperatures without material evaporation. The different thermal treatments applied to each sample are summarized in Table 1.

For each annealed sample, we performed several characterization measurements: EDX to monitor any change in stoichiometry, AFM to study the variation in surface roughness, Raman spectroscopy for structural analysis, and prism-coupling technique to measure both the refractive index and the thickness of thin-films.

3.1.   Elemental composition

When applying thermal treatments to chalcogenide glass thin-films, it is necessary to avoid material loss due to evaporation/sublimation. In order to determine if thin-films undergo any stoichiometric variation, we conducted a compositional analysis by Energy Dispersive X-ray spectroscopy (EDX) for each thermally treated sample: results are presented in Fig. 1(a,b).
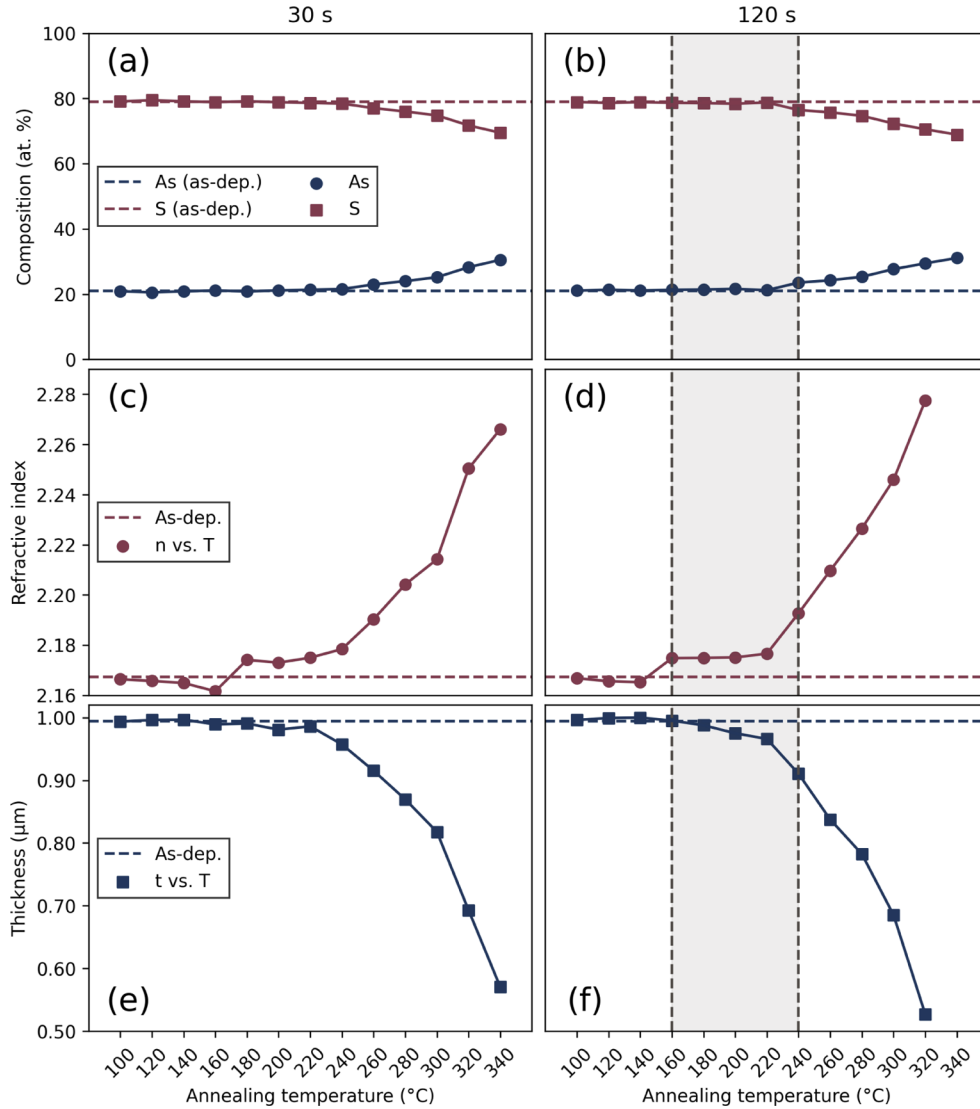

Fig. 1. Thin-films characterisations. (a) and (b): EDX measurements as a function of temperature for 30 s and 120 s annealing durations, respectively. (c) and (d): refractive index of thin-films annealed for 30 s and 120 s, respectively. (e) and (f): thickness versus temperature for samples annealed during 30 s and 120 s, respectively. Dashed lines represent values for the as-deposited thin-film.

It is clear from Fig. 1(a,b) that annealing samples above 240 °C causes sulfur concentration to decrease. $As_{20}S_{80}$ thin-films are composed of several sulfur-rich components such as S_8 rings or S_n chains, which evaporate when temperature increases. Furthermore, As–S thin-films have a

high tendency towards surface crystallization of As_2O_3 whose sublimation temperature is in the 150–200 °C range [28]. Hence, with sulfur loss, the stoichiometry of the thin-film tends to evolve towards that of $As_{40}S_{60}$ which is the more stable composition of the As–S system. According to the results presented in Fig. 1(a,b), thermal treatments performed at $T>240°C$ should be avoided in order to limit sulfur losses.

3.2. Refractive index and thickness

We used the prism-coupling technique to determine the refractive index and the thickness of each sample. As previously presented in section 3.1, when thin-films are annealed at high temperature, a material evaporation can occur. The thickness measurement is used corroborate the range of temperature at which sulfur evaporates, as measured from the EDX (see Section 3.1).

Figure 1(e,f) presents the thickness variation as a function of temperature for $As_{20}S_{80}$ thin-films annealed during (e) 30 s and (f) 120 s. When temperature reaches ~240 °C, the thickness of the film starts to decrease, which is in agreement with results observed in EDX measurements (Fig. 1(a,b)) and Raman scattering spectra (Fig. 2), where sulfur evaporation occurs for temperatures above 240 °C. For higher temperatures, samples thicknesses start to dramatically decrease until almost the entire thin-film has been evaporated. The sample annealed at 340 °C for 120 s had evaporated a lot and the remaining thin-film was too small in area to be measured accurately via the prism-coupling technique.

Concerning refractive index measurements (Fig. 1(c,d)), we observe a slight increase in refractive index at 180 °C (30 s) and 160 °C (120 s): the energy supplied by the thermal treatment is enough to relax the thin-film structure to that of the bulk, as is confirmed by Raman measurements in Section 3.3. For $T>240°C$, the change in stoichiometry caused by sulfur evaporation leads to a substantial increase in refractive index.

We determined that thermal treatments must be performed in the range 160–240 °C in order to limit stoichiometric changes, avoid too much material evaporation, and sufficiently relax the constrained thin-film structure. Figure 1(b,d,f) shows the optimal range in temperatures as a grey filled area.

3.3. Structural analysis

Additionally, we performed a Raman analysis on all samples as a function of thermal treatment temperature and duration. Figure 2 presents Raman spectra of the annealed samples.

During thin-film depositions, a very high temperature gradient is created between the evaporation source and the deposition substrate, thus creating a high quenching speed necessary for glass formation. While a high quenching speed is useful for the formation of otherwise impossible glasses, it generates significant stresses inside the deposited thin-film. These internal constraints can easily be detected through Raman scattering: Fig. 2(f) shows the Raman spectra of an as-deposited thin-film containing internal stresses, and a stress-free bulk glass of $As_{20}S_{80}$.

In Section 3.2, we determined that the optimal range in temperature is 160–240 °C. Raman spectra presented in Fig. 2 further confirm this range: from Fig. 2(d) we can see the temperature needs to be greater than or equal to 160 °C in order to release internal stresses; in Fig. 2(b,c,e), bands associated to sulfur-rich structures (153, 219, 445, 461, 472, and 494 cm^{-1}) start to decrease for $T>240°C$. Figure 3 presents a deconvolution of the as-deposited $As_{20}S_{80}$ thin-film spectrum, using pure Gaussian curves. A list of all the peaks as well as their corresponding vibrations can be found in Table 2.

3.4. Roughness

As previously stated, in order to decrease optical losses, we need to significantly reduce surface and interface roughness. We monitored the roughness of all samples with the help of atomic force microscopy (AFM), using the calculated root mean squared roughness (R_q) as well as the
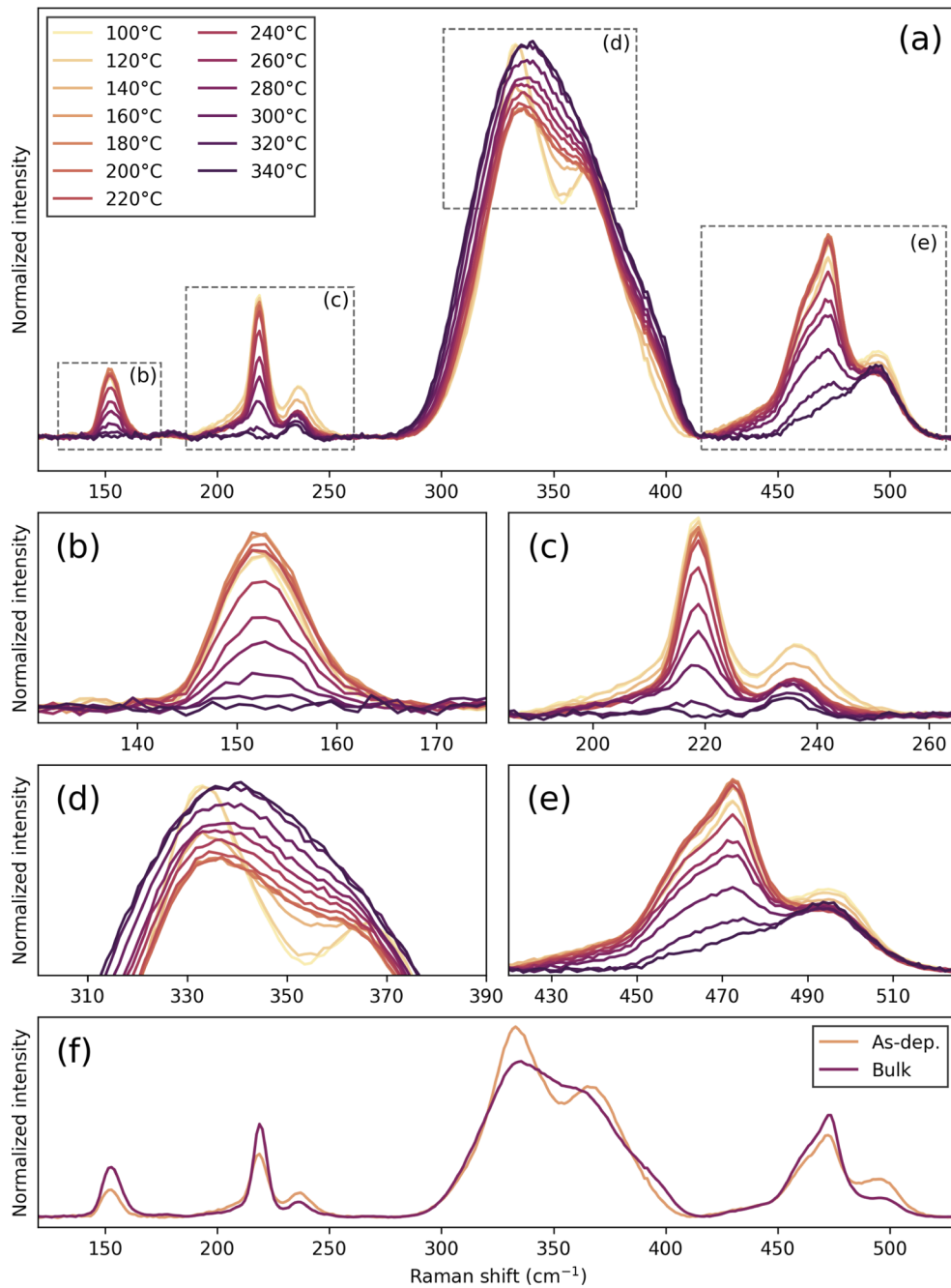
Fig. 2. (a) Raman spectra of $As_{20}S_{80}$ annealed for 120 s at different temperatures. (b,c,d,e): zoom-in of regions of interest. (f) Raman spectra of the bulk and as-deposited $As_{20}S_{80}$ thin-film.
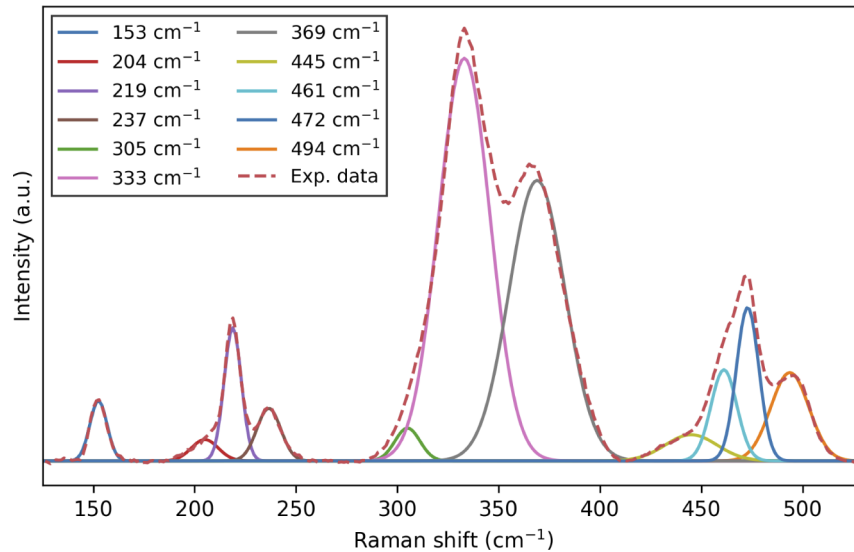
Fig. 3. (top): Raman deconvolution by Gaussian curves of the as-deposited $As_{20}S_{80}$ thin-film.

Table 2. Raman frequencies of $As_{20}S_{80}$.

Peak frequency	Approximate vibration type description	Ref.
$153\,cm^{-1}$	Asymmetric S–S bond bending of S_8 ring structures	[29,30]
$204\,cm^{-1}$	As–As–S bond bending	[31]
$219\,cm^{-1}$	Symmetric S–S bond bending of S_8 ring structures	[29,30]
$237\,cm^{-1}$	As–As–S bond bending	[31]
$305\,cm^{-1}$	As–S symmetric stretching mode	[32]
$333\,cm^{-1}$	Symmetric stretching mode of $AsS_{3/2}$ pyramids	[33]
$369\,cm^{-1}$	Asymmetric stretching mode of $AsS_{3/2}$ pyramids	[33]
$445\,cm^{-1}$	S–S stretching modes	[29]
$461\,cm^{-1}$	Symmetric S–S bond stretching of S_n chains	[30]
$472\,cm^{-1}$	Symmetric S–S bond stretching of S_8 ring structures	[30,34]
$494\,cm^{-1}$	S_2 disulfide bonds	[35]

arithmetic average roughness (R_a), extracted from AFM measurements performed on an area of $1\,\mu m^2$. The extracted values of R_q and R_a are presented in Fig. 4(a,b) for annealing durations of 30 s and 120 s. Examples of surface topography versus thermal treatment temperature are given in Fig. 4(c-f) for samples annealed during 120 s.

As Fig. 4 suggests, annealing samples above the glass transition temperature of $T_g = \sim 100\,°C$ for 120 s seems to slightly reduce surface roughness. As the temperature is increased, R_q and R_a start to exponentially reduce until a constant value of 2 Å is reached for temperatures above 180 °C. This large reduction in roughness is caused by the decrease in viscosity due to the transition from the glassy to the supercooled liquid state, thus smoothing via surface tension [36].

By examining data from the different characterisation techniques presented in Section 3.1, 3.2, 3.3, and 3.4 we determined that the optimal temperature range for thermal treatments is 180 °C–240 °C. However, to apply dewetting to integrated devices we must also consider the kinetics of the phenomenon; we selected an annealing duration of 120 s and temperatures of
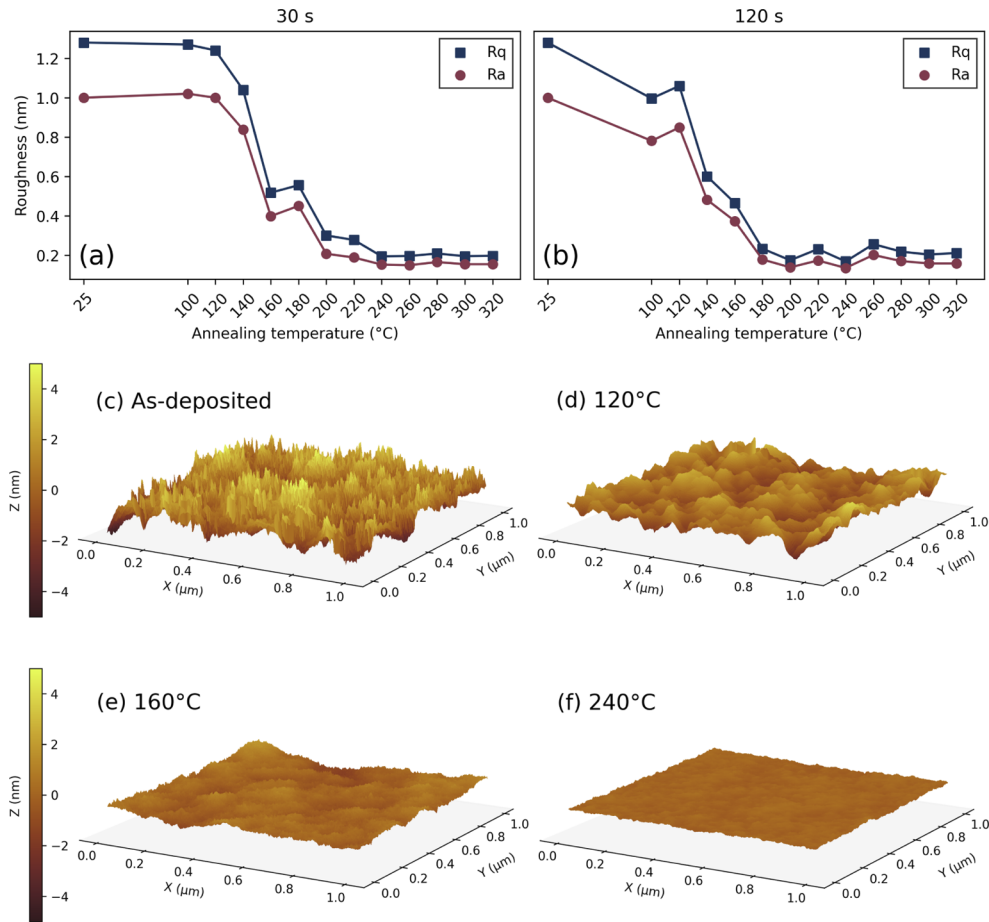
Fig. 4. (a,b) R_q and R_a roughnesses of $As_{20}S_{80}$ thin-films annealed for 30 s and 120 s, respectively. (c-f) Surface topology measured by AFM for the as-deposited thin-film and samples annealed during 120 s at 120 °C, 160 °C, and 240 °C, respectively. The z-axis scale is common to all four 3D graphs.

220 °C, 230 °C, and 240 °C — the highest temperatures possible while maintaining thin-films properties such as thickness and stoichiometry.

4. Templated solid-state dewetting for integrated photonics

This section introduces the concept of templated solid-state dewetting and its application to integrated photonics. The use of dewetting on waveguides fabricated by standard lithography and etching, albeit interesting, is unlikely to satisfy the tight tolerances of modern integrated photonics. In fact, the sensitivity of dewetting to small defects in the film will lead to unwanted geometrical variations, reducing the long-range uniformity and reproducibility. Moreover, matter diffusion during dewetting changes the dimensions of the waveguide, which puts a strict limit on closeness between devices and on the minimum feature size.

To circumvent these problems and to better control the dewetting dynamics, pre-patterned waveguide templates are used. To do so, micro-trenches are directly etched in the top silicon dioxide claddings of standard 220 nm silicon-on-insulator chips and filled with chalcogenide,

corresponding to step 1 and 2 as shown in Fig. 5(a). The fabrication process is completed by a high-temperature annealing to induce dewetting (see Experimental section). The fabricated chalcogenide structures can be evanescently coupled to the silicon waveguides [37]. The geometry of the hybrid chalcogenide-silicon microresonator is visible on the top view micrographs of Fig. 5(b). We note that this approach could be generalized in a monolithic chalcogenide platform without silicon where the micro-trench would be defined directly in the thermal oxide layer of oxidized silicon wafers [38].
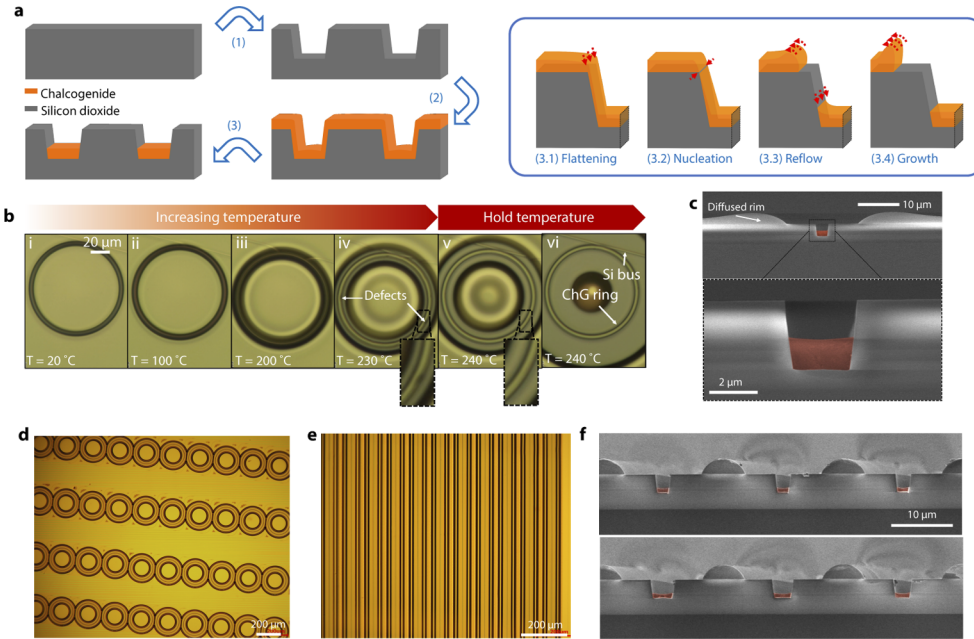

Fig. 5. Templated solid-state dewetting of chalcogenide films around micro-trenches. (a) Left panel: simplified schematic of the fabrication steps. The chalcogenide and silicon dioxide films are shown in orange and grey, respectively. The silicon substrate is not illustrated for clarity. Right panel: schematic of the dewetting dynamics around the micro-trench, separated in four steps (flattening, nucleation, reflow and growth). (b) Micrographs showing the evolution of the dewetting process. The heating rate is $100\,°C·min^{-1}$ and the final temperature is $240\,°C$. The insets iv and v shows the disappearance of a defect during dewetting. (c) SEM cross-section of a waveguide, the diffused rim is visible and approximately retracted by $5\,µm$ from the micro-trench. The waveguide core is false colored orange for visibility. (d) and (e) Arrays of microring resonators and straight waveguides showing mm-range (die-scale) uniformity of the dewetting process. (f) SEM cross-section of adjacent waveguides with widths ranging from $1.5\,µm$ to $4.0\,µm$. Again, the diffused rims are visible between the waveguides.

The dynamics of dewetting in micro-trench waveguides can be described in four steps: flattening, nucleation, reflow and growth (right panel of Fig. 5(a)). As the temperature increases beyond T_g, the glass viscosity falls off rapidly, causing a flattening of the film through curvature-driven self-diffusion. At the top corner of the trench, this flattening leads to a thinning of the film. If the film is thin enough, its surface will eventually meet with the substrate surface to form a hole (nucleation, 3.2). This hole then grows through a combination of rim self-diffusion and reflow along the trench sidewall.

A few micrographs taken during the process are shown in Fig. 5(b). The dewetting starts at nucleation when there is sufficient energy to break the film metastability (around $T_g + 80\,°C$ in

this case) and continue with increasing temperature. The full video is provided in Visualization 1. The glass will continue to dewet even after the temperature stops to increase; the dewetting will only stop when the temperature is reduced again. Interestingly, the spontaneous matter reorganization can remove defects present on the film. This is visible in the insets of panels iv and v of Fig. 5(b). It is also expected that nanometer scale defects in the film would be smoothed out in a similar manner. This effect was quantified in Section 3.4.

The resulting waveguides have well-defined, uniform rectangular cross-sections, as visible in Fig. 5(c) and (f). This is due to the use of a template, as waveguides left to dewet without template would result in rounded, difficult to predict shapes. The template forces the matter into the desired shape. The dewetting is only partial, given enough thermal energy, it would be expected that even the flat sections of the films would breakup due to small random density fluctuations. The use of a templated substrate, a fast heating rate, and a short duration at maximum temperature favor nucleation and growth instead of spinodal dewetting, which would result in randomly organized island patterns [10,39,40]. At the die-level (mm scale), the waveguides and components visually retain their shape and are very uniform, as visible on Fig. 5(d) and (e). It is important to emphasize that this uniformity is crucial for the practical use of dewetting and could not be achieved without pre-patterned templates.

4.1. Process versatility

To showcase the process versatility, various microresonators (MRs) were fabricated and tested. MRs are interesting to benchmark a fabrication technique as they provide direct measurement of the relevant information (propagation loss and dispersion). MRs are also versatile; depending on their constituent materials, they can be used as lasers [41], sensors [42], filters [43] or modulators [44], to name only a few. As such, they find use in various fields like telecommunications, nonlinear optics, quantum optics, and metrology. This ubiquity motivated our choice to focus on these structures. We selected three types of microresonators for demonstration: microring resonators (MRRs) (Fig. 6(a)), microdisk resonators (MDRs) (Fig. 6(d)) and racetrack resonators (RTRs) (Fig. 6(f)). The MRRs and RTRs shown in Fig. 6 are based on waveguides with a width of $2.5\,\mu m$ and a thin-film thickness of $1\,\mu m$. The chips were annealed at $240\,°C$ for $120\,s$ to induce dewetting. All the resonators were directly coupled to $220\,nm$ thick silicon waveguides for characterization.

We fabricated and tested MRRs with different radius from $5\,\mu m$ to $100\,\mu m$. As expected, the increase in radius and optical path length comes with a monotonic decrease of the free-spectral range (FSR), as shown in Fig. 6(b) and (c). Another important result is the effect of radius on propagation loss α. Increasing the waveguide curvature leads to additional loss through leakage of the optical mode outside of the core and increasing interaction with the sidewall roughness. The radius at which bending loss becomes unacceptable dictates the integration density of the platform (i.e. the minimum footprint of devices), a crucial figure of merit in integrated photonics. The bending losses of the MRR become high ($>1\,dB\cdot cm^{-1}$) for $R < 10\,\mu m$ (see Fig. 6(c) bottom panel). At $R = 5\,\mu m$, α is $5.8\,dB\cdot cm^{-1}$. These results highlights the suitability of these devices for densely integrated photonics. The propagation loss decreases rapidly for large radius; α reduces to $0.43\,dB\cdot cm^{-1}$ for $R = 50\,\mu m$ and then to a minimum of $0.38\,dB\cdot cm^{-1}$ for $R = 100\,\mu m$. This corresponds to an intrinsic quality factor of about 1×10^6.

MDRs and RTRs were also fabricated and characterized (see Fig. 6(d) through (g). Typical normalized transmittance spectrum are shown in Fig. 6(e) and (g). The longer path length of RTR resulted in a much smaller FSR of about $50\,GHz$ ($0.65\,nm$) at $1.6\,\mu m$. The RTRs are based on the same waveguide as the MRRs. The MDR, on the other hand, uses micro-trenches with a missing sidewall, or a very large width, which results in multimode behavior (see Fig. 6(e)). It could be expected that such a wide trench would result in a different dewetting behavior, mainly a dislocation of the glass from the sidewall [45]. This effect was not observed during this study
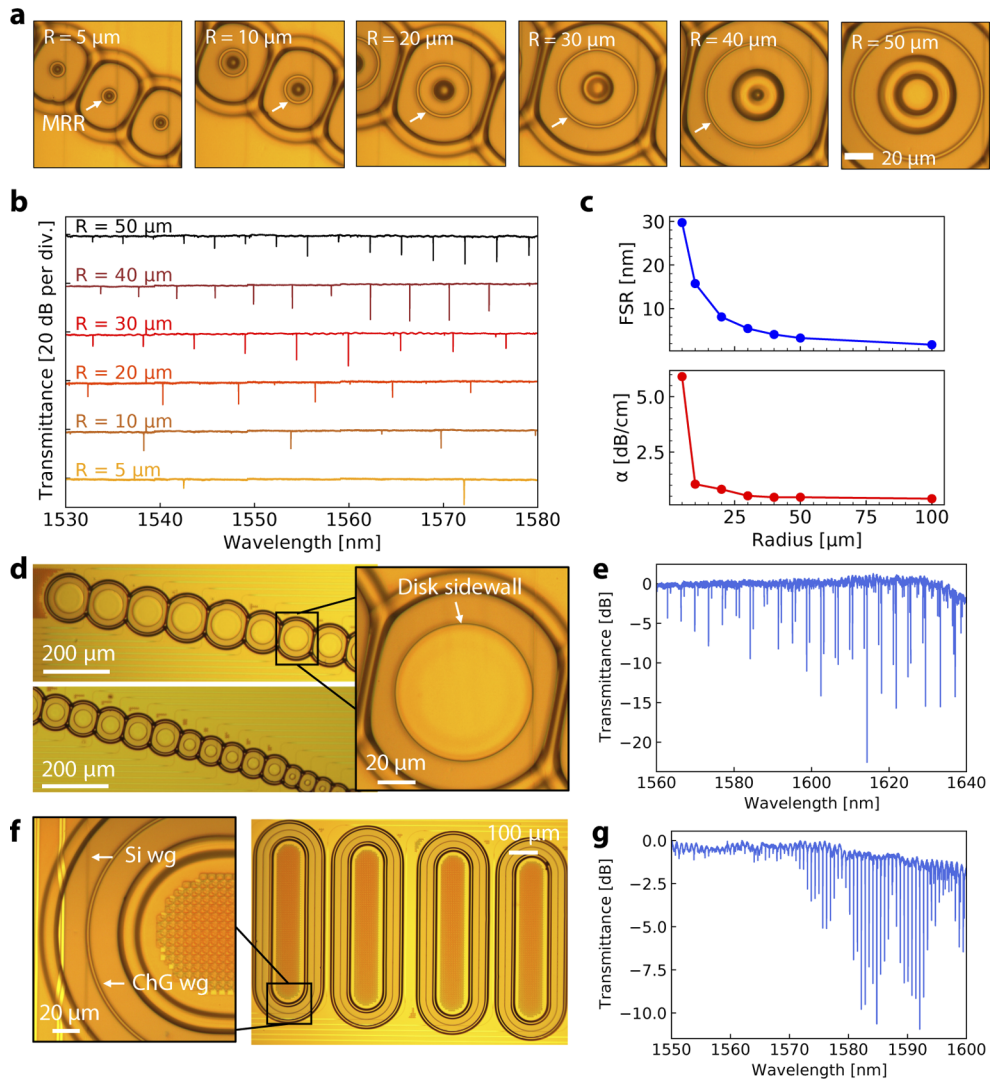
Fig. 6. Process versatility for integrated photonics. (a) Top view micrographs of microring resonators with increasing radius (from left to right: 5 μm, 10 μm, 20 μm, 30 μm, 40 μm and 50 μm). The white arrow shows the position of the microring resonator (MRR). (b) Normalized transmittance of the microring resonators. (c) Top panel: FSR as a function of ring radius. Bottom panel: propagation loss α as a function of ring radius. (d) Left panel: Top view micrographs of microdisk resonators with varying radius. Right panel: close-up view of a single microdisk, the slight variation of color indicates a change of thickness across the trench. (e) Normalized transmittance of a microdisk resonator with $R = 50$ μm. (f) Left panel: top view micrographs of racetrack resonators. Right panel: close-up view of the coupling section. The silicon bus waveguide (Si wg) and chalcogenide waveguide (ChG wg) are identified. (g) Normalized transmittance of the racetrack resonator.

because of the partial and well controlled dewetting process. However, we observed a thickness gradient in the microdisk trench, as visible from the slight color variations on the inset of Fig. 6(d). It is expected that if the higher temperature or longer time were used, spinodal dewetting shapes would form inside the microdisk.

4.2. Towards ultra-high-Q glass microresonators

In this section, we show the advantage of using dewetting to achieve ultra-smooth microdisks with high quality factor. The previous sections showed that various integrated photonics components can benefit from dewetting, highlighting the versatility of the technique. However, the moderate quality factor $Q \sim 1 \times 10^6$ achieved in microrings suggest the presence of a significant loss channel. The main loss mechanism in microrings and racetracks is believed to be scattering from the silicon dioxide sidewall, an artefact from the foundry processing that could obscure the real potential of the dewetting technique. Microdisk resonators have a single SiO_2 sidewall to interact with the optical mode, making them less susceptible to this roughness scattering.

The microdisk annealed at 230 °C showed the highest Q. The resulting microdisk structure is presented in Fig. 7(a). In this case, dewetting was found to be significantly less aggressive than
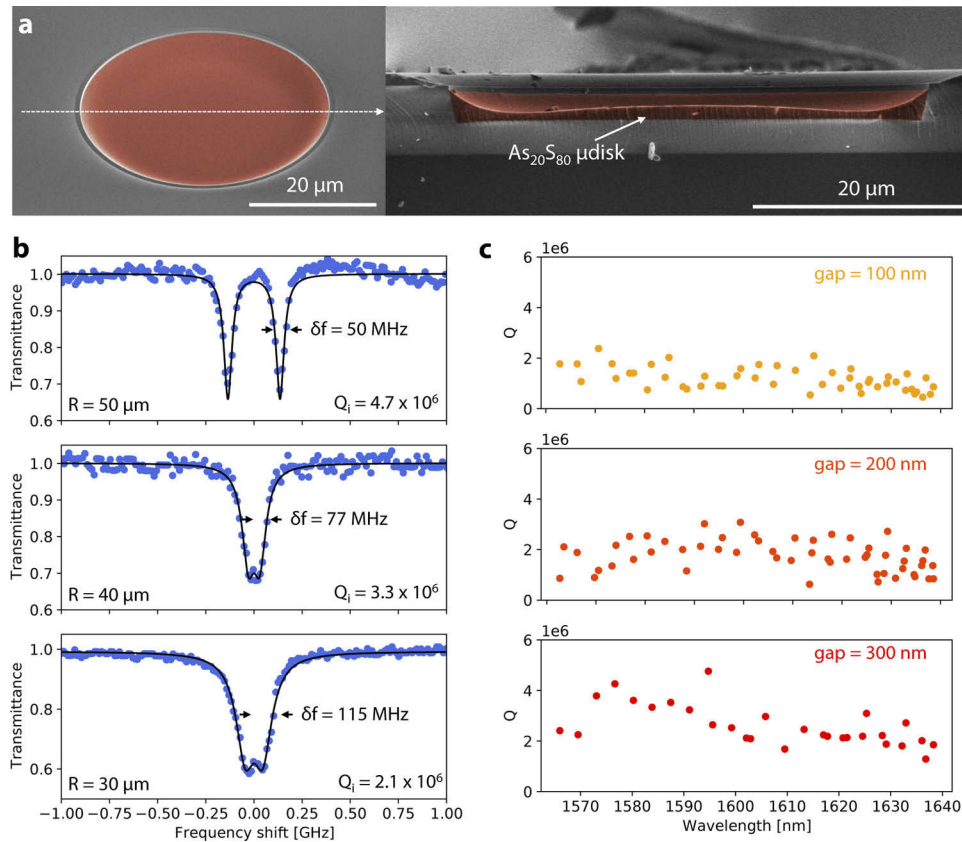

Fig. 7. High-Q in microdisk resonators. (a) Left panel: top view SEM images of a microdisk with modest dewetting. Right panel: Cross-section of the microdisk. (b) Measured resonance (blue dots) and Lorentzian fit (black line) for MDR with (top) $R = 50\,\mu m$, (middle) $R = 40\,\mu m$ and (bottom) $R = 30\,\mu m$. The corresponding intrinsic Q are 4.7×10^6, 3.3×10^6 and 2.1×10^6. (c) Measured Q from 1560 nm to 1640 nm in MDR with $R = 50\,\mu m$ and different gaps (from top to bottom: 100 nm, 200 nm and 300 nm).

for the 220 °C treatment. The extracted quality factor (see experimental section) are summarized in Fig. 7(b) for a few geometries. The Q exceeds 1×10^6 for all microdisk variations. The absolute maximum value of $Q = 4.7 \times 10^6$ was observed in the largest device ($R = 50\,\mu$m) with the weakest coupling ($g = 300$ nm). Quality factors of up to 3.3×10^6 and 2.1×10^6 were also measured for radius of 40 µm and 30 µm, respectively.

Higher quality factors are achieved in the microdisks with weaker coupling (larger g), suggesting a dependence of Q on the distance between the silicon bus waveguide and the micro-trench. This could be explained by a stronger interaction of the disk optical mode with the bus waveguide as the gap is narrowed. The propagation loss in the 400 nm wide silicon bus waveguide could reach tens of dB/cm [46]. Because of these high losses, even a minute increase in the interaction could result in an observable effect such as the one visible on Fig. 7(c).

We note that the change in annealing temperature made little difference for the other structures (MRR and RTR). In addition, comparable values of Q were obtained for microdisks annealed at 220 °C for 120 s (not shown here). We did not investigate lower temperatures as the dewetting becomes negligible in those cases. The difference between the quality factor in the MRR (1×10^6) and the MDR (4.7×10^6) suggests that scattering from the sidewall roughness in the micro-trench is a primary source of loss. This can be inferred since light in the MRR has significantly more surface roughness to interact with because of the presence of two sidewalls. If the film absorption was the limiting factor, the difference between the MRR and MDR would not be so stark. This also indicates that the short BOE treatment did not reduce the roughness sufficiently. Since the highest Q was measured in the largest radius device with the weakest coupling, it would be worthwhile to investigate the effect of increasing the radius beyond 50 µm.

5. Discussion

At this point, a comparison with existing high-Q demonstrations in the literature is worthwhile. Such a comparison with state-of-the-art silicon and chalcogenide microresonators is provided in Table 3. The main point to emphasize is that while higher quality factors have been achieved in both silicon and chalcogenide (As_2S_3), these demonstrations relied on extremely low-confinement waveguides requiring mm-scale bend radius, making them unsuitable for dense integration, one of the major fundamental advantages of integrated photonics. In contrast, the microdisk reported in this work shows a high-Q without compromising density. To quantify this and to directly compare demonstrations, we used the ratio Q/R as a figure of merit (FOM). The advantage of the dewetted microdisk becomes obvious here, where only slab silicon microdisks provide a better tradeoff between loss and compactness. Furthermore, the monolithic integration of the microdisk on the SOI platform makes them attractive for practical applications as they can be readily coupled to existing systems. They can also be interfaced with optical fibers using existing high-performance silicon couplers [47].

Table 3. Comparison of high-Q demonstrations on silicon/chalcogenide

Material	Q	R	Q/R	SOI	Ref.
		[µm]	[µm^{-1}]	Y/N	
Silicon	2.2×10^7	2.45×10^3	9000	Yes	[48]
Silicon	3×10^6	20	150,000	Yes	[49]
As_2S_3	1.44×10^7	2.47×10^3	5800	No	[19]
$Ge_{25}Sb_{10}S_{65}$	2.2×10^6	100	22,000	No	[18]
$As_{20}S_{80}$	4.7×10^6	50	94,000	Yes	This work

The surface roughness of the chalcogenide film after dewetting is $R_q = 0.189$ nm (see Fig. 8). This confirms that scattering from the chalcogenide film surface is not a significant loss channel.

However, the bottom surface of the micro-trench had significant roughness; a relatively high R_q of 1.6 nm was measured on the as-delivered chips and was only reduced to $R_q = 1.43$ nm after the BOE treatment (see Fig. 8). Scattering from the bottom surface of the waveguide (interface between the bottom of the trench and the chalcogenide core) could then contribute to the overall loss of the device. We were not able to directly measure the roughness of the etched sidewalls, but it is possible to infer that it is at least higher than the roughness at the bottom of the trench. The SiO$_2$ passivation film was relatively smooth with $R_q = 0.559$ nm. We conclude that reducing both the sidewall and surface roughness of the silicon dioxide layer, either using an optimized etching process or a polishing step, could improve the Q beyond what was measured in this work. We emphasize that the achieved value of $R_q = 0.189$ nm indicates atomic-scale roughness, suggesting a path towards ultra-high-Q ($Q > 10^7$) integrated devices.
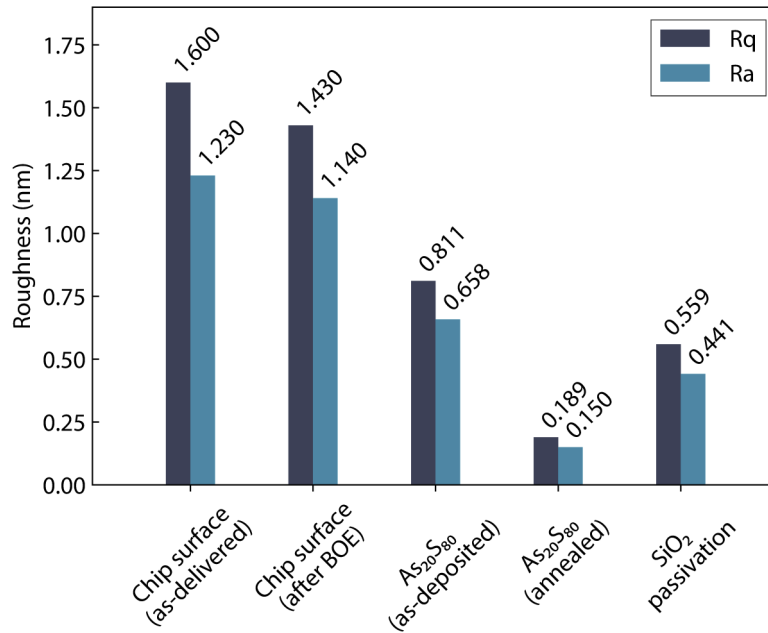

Fig. 8. Surface roughness of the microdisk at different fabrication steps. The label "Chip surface" refers to the silicon dioxide at the bottom of the micro-trench before the chalcogenide thin-film deposition. The label "As$_{20}$S$_{80}$ refers to the chalcogenide thin-film surface. The label "SiO$_2$ passivation" refers to the passivation layer deposited on top of the chalcogenide thin-film.

Another important factor to consider regarding ultra-high-Q devices is the material background absorption, which would ultimately limit the achievable Q given perfect fabrication. We did not measure the background absorption of As$_{20}$S$_{80}$ thin-films. A comparison with the commonly used As$_{40}$S$_{60}$ can be informative; the lowest loss obtained from optical fibers is 0.9 dB·m^{-1} [50]. We can suppose that the lower bound of thin-film loss is comparable to the optical fiber value. Based on the Q of the MDR, we obtain a propagation loss of $\alpha = 0.08$ dB·cm^{-1} (8 dB·m^{-1}). Considering the order of magnitude difference between the theoretical limit and measured value in microdisks, these devices are unlikely to be limited by material absorption. However, the value of $\alpha = 0.08$ dB·cm^{-1} can be used as an upper bound on the thin-film propagation loss, confirming that dewetting does not cause excessive optical losses.

6.   Conclusion

In summary, we presented the results of an in-depth study of $As_{20}S_{80}$ thin-film dewetting and its application for integrated photonics. One of the main interests of the method is the achieved smoothness of the film ($R_q < 2$ Å) without the need of more complex processes like wet etching or chemical-mechanical polishing. This technique of dewetting is promising for enabling compact, ultra-high-Q planar microresonators. In microdisk, we reported a Q of 4.7×10^6, the highest value to date for a planar chalcogenide microresonator. Further loss reduction will require improvement of the micro-trench processing. The methods reported in this work could also be generalized to several other materials, including various chalcogenide compositions, polymers [51], metals [52] and oxide glasses [53].

The novel idea of defining optical structures by spontaneous matter reorganization could provide a path for simpler and cheaper fabrication paradigms and lead to improvement of standard fabrication process. This work establish the basis for the use of templated dewetting for the fabrication of high-performance hybrid chalcogenide/silicon integrated photonics components.

Disclosures. The authors declare no conflicts of interest.

Data availability. Data underlying the results presented in this paper are not publicly available at this time but may be obtained from the authors upon reasonable request.

References

1. J. Wang, S. Paesani, Y. Ding, R. Santagati, P. Skrzypczyk, A. Salavrakos, J. Tura, R. Augusiak, L. Mančinska, D. Bacco, D. Bonneau, J. W. Silverstone, Q. Gong, A. Acín, K. Rottwitt, L. K. Oxenløwe, J. L. O'Brien, A. Laing, and M. G. Thompson, "Multidimensional quantum entanglement with large-scale integrated optics," Science **360**(6386), 285–291 (2018).
2. W. Shi, Y. Tian, and A. Gervais, "Scaling capacity of fiber-optic transmission systems via silicon photonics," Nanophotonics **9**(16), 4629–4663 (2020).
3. J. Wang, F. Sciarrino, A. Laing, and M. G. Thompson, "Integrated photonic quantum technologies," Nat. Photonics **14**(5), 273–284 (2020).
4. M. W. Puckett, K. Liu, N. Chauhan, Q. Zhao, N. Jin, H. Cheng, J. Wu, R. O. Behunin, P. T. Rakich, K. D. Nelson, and D. J. Blumenthal, "422 million intrinsic quality factor planar integrated all-waveguide resonator with sub-mhz linewidth," Nat. Commun. **12**(1), 934 (2021).
5. J. Liu, G. Huang, R. N. Wang, J. He, A. S. Raja, T. Liu, N. J. Engelsen, and T. J. Kippenberg, "High-yield, wafer-scale fabrication of ultralow-loss, dispersion-engineered silicon nitride photonic circuits," Nat. Commun. **12**(1), 2236 (2021).
6. X. Ji, F. A. S. Barbosa, S. P. Roberts, A. Dutt, J. Cardenas, Y. Okawachi, A. Bryant, A. L. Gaeta, and M. Lipson, "Ultra-low-loss on-chip resonators with sub-milliwatt parametric oscillation threshold," Optica **4**(6), 619–624 (2017).
7. M. Belt, M. L. Davenport, J. E. Bowers, and D. J. Blumenthal, "Ultra-low-loss Ta_2O_5-core/SiO_2-clad planar waveguides on Si substrates," Optica **4**(5), 532–536 (2017).
8. S. Roberts, X. Ji, J. Cardenas, M. Corato-Zanarella, and M. Lipson, "Measurements and modeling of atomic-scale sidewall roughness and losses in integrated photonic devices," (2021).
9. M. H. P. Pfeiffer, J. Liu, A. S. Raja, T. Morais, B. Ghadiani, and T. J. Kippenberg, "Ultra-smooth silicon nitride waveguides based on the Damascene reflow process: fabrication and loss origins," Optica **5**(7), 884 (2018).
10. A. Douaud, S. H. Messaddeq, and Y. Messaddeq, "Microstructure formation in chalcogenide thin films assisted by thermal dewetting," J. Mater. Sci.: Mater. Electron. **28**(10), 6989–6999 (2017).
11. D. Gentili, G. Foschi, F. Valle, M. Cavallini, and F. Biscarini, "Applications of dewetting in micro and nanotechnology," Chem. Soc. Rev. **41**(12), 4430 (2012).
12. D. K. Armani, T. J. Kippenberg, S. M. Spillane, and K. J. Vahala, "Ultra-high-Q toroid microcavity on a chip," Nature **421**(6926), 925–928 (2003).
13. M. L. Gorodetsky, A. A. Savchenkov, and V. S. Ilchenko, "Ultimate Q of optical microsphere resonators," Opt. Lett. **21**(7), 453–455 (1996).
14. T. Das Gupta, L. Martin-Monier, W. Yan, A. Le Bris, T. Nguyen-Dang, A. G. Page, K.-T. Ho, F. Yesilköy, H. Altug, Y. Qu, and F. Sorin, "Self-assembly of nanostructured glass metasurfaces via templated fluid instabilities," Nat. Nanotechnol. **14**(4), 320–327 (2019).
15. B. J. Eggleton, B. Luther-Davies, and K. Richardson, "Chalcogenide photonics," Nat. Photonics **5**(3), 141–148 (2011).

16. P. Jean, A. Douaud, V. Michaud-Belleau, S. H. Messaddeq, J. Genest, S. LaRochelle, Y. Messaddeq, and W. Shi, "Etchless chalcogenide microresonators monolithically coupled to silicon photonic waveguides," Opt. Lett. **45**(10), 2830–2833 (2020).

17. J. Hu, N.-N. Feng, N. Carlie, L. Petit, A. Agarwal, K. Richardson, and L. Kimerling, "Optical loss reduction in high-index-contrast chalcogenide glass waveguides via thermal reflow," Opt. Express **18**(2), 1469–1478 (2010).

18. Y. Huang, D. Xia, P. Zeng, J. Zhao, Z. Yang, S. Sun, L. Luo, G. Hu, D. Liu, Y. Li, H. Guo, B. Zhang, and Z. Li, "Engineered raman lasing in photonic integrated chalcogenide microresonators," (2021).

19. D.-G. Kim, S. Han, J. Hwang, I. H. Do, D. Jeong, J.-H. Lim, Y.-H. Lee, M. Choi, Y.-H. Lee, D.-Y. Choi, and H. Lee, "Universal light-guiding geometry for on-chip resonators having extremely high q-factor," Nat. Commun. **11**(1), 5933 (2020).

20. Y. Zhang, J. B. Chou, J. Li, H. Li, Q. Du, A. Yadav, S. Zhou, M. Y. Shalaginov, Z. Fang, H. Zhong, C. Roberts, P. Robinson, B. Bohlin, C. Ríos, H. Lin, M. Kang, T. Gu, J. Warner, V. Liberman, K. Richardson, and J. Hu, "Broadband transparent optical phase change materials for high-performance nonvolatile photonics," Nat. Commun. **10**(1), 4279 (2019).

21. Y. Yu, X. Gai, T. Wang, P. Ma, R. Wang, Z. Yang, D.-Y. Choi, S. Madden, and B. Luther-Davies, "Mid-infrared supercontinuum generation in chalcogenides," Opt. Mater. Express **3**(8), 1075–1086 (2013).

22. M. Galili, J. Xu, H. C. Mulvad, L. K. Oxenløwe, A. T. Clausen, P. Jeppesen, B. Luther-Davies, S. Madden, A. Rode, D.-Y. Choi, M. Pelusi, F. Luan, and B. J. Eggleton, "Breakthrough switching speed with an all-optical chalcogenide glass chip: 640 gbit/s demultiplexing," Opt. Express **17**(4), 2182–2187 (2009).

23. X. Gai, T. Han, A. Prasad, S. Madden, D.-Y. Choi, R. Wang, D. Bulla, and B. Luther-Davies, "Progress in optical waveguides fabricated from chalcogenide glasses," Opt. Express **18**(25), 26635–26646 (2010).

24. P. E. Barclay, K. Srinivasan, and O. Painter, "Nonlinear response of silicon photonic crystal microresonators excited via an integrated waveguide and fiber taper," Opt. Express **13**(3), 801–820 (2005).

25. L. W. Luo, G. S. Wiederhecker, J. Cardenas, and M. Lipson, "High quality factor etchless silicon photonic ring resonators," Opt. Express **19**(7), 6284 (2011).

26. P. Rabiei, W. H. Steier, C. Zhang, and L. R. Dalton, "Polymer micro-ring filters and modulators," J. Lightwave Technol. **20**(11), 1968–1975 (2002).

27. A. Li, T. Van Vaerenbergh, P. De Heyn, P. Bienstman, and W. Bogaerts, "Backscattering in silicon microring resonators: a quantitative analysis," Laser Photonics Rev. **10**(3), 420–431 (2016).

28. F. Cuypers, C. De Dobbelaere, A. Hardy, M. K. Van Bael, and L. Helsen, "Thermal behaviour of arsenic trioxide adsorbed on activated carbon," J. Hazard. Mater. **166**(2-3), 1238–1243 (2009).

29. C. Nims, B. Cron, M. Wetherington, J. Macalady, and J. Cosmidis, "Low frequency Raman spectroscopy for micron-scale and in vivo characterization of elemental sulfur in microbial samples," Sci. Rep. **9**(1), 7971 (2019).

30. A. G. Kalampounias, K. S. Andrikopoulos, and S. N. Yannopoulos, "Probing the sulfur polymerization transition in situ with Raman spectroscopy," J. Chem. Phys. **118**(18), 8460–8467 (2003).

31. P. Bonazzi, S. Menchetti, G. Pratesi, M. Muniz-Miranda, and G. Sbrana, "Light-induced variations in realgar and beta -As_4S_4: X-ray diffraction and Raman studies," Am. Mineral. **81**(7-8), 874–880 (1996).

32. H. Cheng, Y. Zhou, and R. L. Frost, "Structure comparison of Orpiment and Realgar by Raman spectroscopy," Spectrosc. Lett. **50**(1), 23–29 (2017).

33. T. Mori, K. Matsuishi, and T. Arai, "Vibrational properties and network topology of amorphous As–S systems," J. Non-Cryst. Solids **65**(2-3), 269–283 (1984).

34. P. D. Harvey and I. S. Butler, "Raman spectra of orthorhombic sulfur at 40 k," J. Raman Spectrosc. **17**(4), 329–334 (1986).

35. F. Kyriazis, A. Chrissanthopoulos, V. Dracopoulos, M. Krbal, T. Wagner, M. Frumar, and S. Yannopoulos, "Effect of silver doping on the structure and phase separation of sulfur-rich As–S glasses: Raman and SEM studies," J. Non-Cryst. Solids **355**(37-42), 2010–2014 (2009).

36. C.-Y. Chao and L. Guo, "Reduction of surface scattering loss in polymer microrings using thermal-reflow technique," IEEE Photonics Technol. Lett. **16**(6), 1498–1500 (2004).

37. P. Jean, A. Douaud, S. T. Bah, S. LaRochelle, Y. Messaddeq, and W. Shi, "Universal micro-trench resonators for monolithic integration with silicon waveguides," Opt. Mater. Express **11**(9), 2753–2767 (2021).

38. C. Li, P. Guo, W. Huang, W. Zhang, P. Xu, and P. Zhang, "Reverse-strip-structure $Ge_{28}Sb_{12}Se_{60}$ chalcogenide glass waveguides prepared by micro-trench filling and lift-off," J. Opt. Soc. Am. B **37**(1), 82–87 (2020).

39. Y. N. Colmenares, S. H. Messaddeq, and Y. Messaddeq, "Studying the kinetics of microstructure formation through dewetting of As-Se thin films," Phys. Rev. Mater. **5**(1), 015605 (2021).

40. Y. N. Colmenares, W. Correr, S. H. Messaddeq, and Y. Messaddeq, "Controlling thermal-induced dewetting of $As_{20}Se_{80}$ thin films for integrated photonics applications," Opt. Mater. Express **11**(6), 1720–1732 (2021).

41. J. D. B. Bradley and E. S. Hosseini, "Monolithic erbium- and ytterbium-doped microring lasers on silicon chips," Opt. Express **22**(10), 12226–12237 (2014).

42. K. D. Vos, I. Bartolozzi, E. Schacht, P. Bienstman, and R. Baets, "Silicon-on-insulator microring resonator for sensitive and label-free biosensing," Opt. Express **15**(12), 7610–7615 (2007).

43. B. Little, S. Chu, H. Haus, J. Foresi, and J.-P. Laine, "Microring resonator channel dropping filters," J. Lightwave Technol. **15**(6), 998–1005 (1997).

Optical Materials EXPRESS

44. R. Dubé-Demers, S. LaRochelle, and W. Shi, "Ultrafast pulse-amplitude modulation with a femtojoule silicon photonic modulator," Optica **3**(6), 622–627 (2016).

45. L.-X. Lu, Y.-M. Wang, B. M. Srinivasan, M. Asbahi, J. K. W. Yang, and Y.-W. Zhang, "Nanostructure formation by controlled dewetting on patterned substrates: A combined theoretical, modeling and experimental study," Sci. Rep. **6**(1), 32398 (2016).

46. W. Bogaerts, R. Baets, P. Dumon, V. Wiaux, S. Beckx, D. Taillaert, B. Luyssaert, J. Van Campenhout, P. Bienstman, and D. Van Thourhout, "Nanophotonic waveguides in silicon-on-insulator fabricated with CMOS technology," J. Lightwave Technol. **23**(1), 401–412 (2005).

47. L. Jia, C. Li, T.-Y. Liow, and G.-Q. Lo, "Efficient suspended coupler with loss less than −1.4 dB between si-photonic waveguide and cleaved single mode fiber," J. Lightwave Technol. **36**(2), 239–244 (2018).

48. A. Biberman, M. J. Shaw, E. Timurdogan, J. B. Wright, and M. R. Watts, "Ultralow-loss silicon ring resonators," Opt. Lett. **37**(20), 4236–4238 (2012).

49. M. Soltani, S. Yegnanarayanan, and A. Adibi, "Ultra-high Q planar silicon microdisk resonators for chip-scale silicon photonics," Opt. Express **15**(8), 4694–4704 (2007).

50. W. Kim, V. Nguyen, L. Shaw, L. Busse, C. Florea, D. Gibson, R. Gattass, S. Bayya, F. Kung, G. Chin, R. Miklos, I. Aggarwal, and J. Sanghera, "Recent progress in chalcogenide fiber technology at NRL," J. Non-Cryst. Solids **431**, 8–15 (2016).

51. H. Zhang, L. Xu, Y. Xu, G. Huang, X. Zhao, Y. Lai, and T. Shi, "Enhanced self-organized dewetting of ultrathin polymer blend film for large-area fabrication of SERS substrate," Sci. Rep. **6**(1), 38337 (2016).

52. M. Oliva-Ramírez, D. Wang, D. Flock, V. Rico, A. R. González-Elipe, and P. Schaaf, "Solid-state dewetting of gold on stochastically periodic SiO_2 nanocolumns prepared by oblique angle deposition," ACS Appl. Mater. Interfaces **13**(9), 11385–11395 (2021).

53. J. Richter, M. P. Nezhad, B. Hadam, T. Taubner, J. Knoch, F. Merget, A. Moscoso-Mártir, and J. Witzens, "High-q inverted silica microtoroid resonators monolithically integrated into a silicon photonics platform," Opt. Express **26**(21), 27418–27440 (2018).